

COMMUNICATION

[View Article Online](#)  
[View Journal](#) | [View Issue](#)



Cite this: *RSC Sustainability*, 2025, **3**, 4457

Received 2nd May 2025  
Accepted 13th August 2025

DOI: 10.1039/d5su00317b

rsc.li/rscsus

Herein we report a green mechanochemical synthesis with low energy input of dual-function materials for integrated  $\text{CO}_2$  capture and dry reforming of methane. The materials produced syngas during the  $\text{CH}_4$  step (up to  $0.6 \text{ mmol g}^{-1}$   $\text{CO}$  and  $7.7 \text{ mmol g}^{-1}$   $\text{H}_2$ ) and  $\text{CO}$  during the  $\text{CO}_2$  step (up to  $3.1 \text{ mmol g}^{-1}$ ) via the reverse Boudouard reaction due to the carbon produced from  $\text{CH}_4$  cracking.

## Introduction

Nowadays, there is an urgent need to deal with the increased carbon dioxide ( $\text{CO}_2$ ) emissions in order to achieve net-zero  $\text{CO}_2$  emissions by 2050 according to the Paris Agreement.<sup>1,2</sup> Atmospheric  $\text{CO}_2$  has increased from *ca.* 270 ppm in the pre-industrial era to 426 ppm in July 2024 with 37.4 Gt of  $\text{CO}_2$  emitted in 2023, reaching a record high.<sup>3–5</sup> Another alarming greenhouse gas is methane ( $\text{CH}_4$ ), which is 25 times more harmful than  $\text{CO}_2$ .<sup>6</sup> In fact, its atmospheric concentration has increased from 715 ppb in the pre-industrial era to 1930 ppb in February 2024,<sup>5,6</sup> and its emissions were 135 Mt in 2022, corresponding to *ca.* 4 Gt of  $\text{CO}_2$  equivalent.<sup>7</sup> As a way of combating the  $\text{CO}_2$  emissions, Carbon Capture and Storage (CCS) and Carbon Capture and Utilisation (CCU) have extensively been studied because  $\text{CO}_2$  can be captured and then either stored in the underground formations or used to form added-value fuels and chemicals.<sup>8–11</sup>

One of the most promising  $\text{CO}_2$  utilisation reactions is dry reforming of methane (DRM), during which  $\text{CO}_2$  reacts with  $\text{CH}_4$  and hence, syngas, *i.e.* a mixture of carbon monoxide ( $\text{CO}$ ) and hydrogen ( $\text{H}_2$ ), is obtained (eqn (1)).<sup>12–15</sup> The stoichiometric  $\text{H}_2/\text{CO}$  ratio is 1, which is useful for the production of long chain hydrocarbons and oxygenated chemicals. However, the

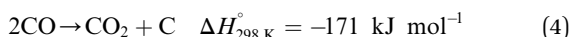
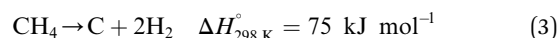
## Integrated carbon capture and dry reforming of methane of mechanochemically synthesised dual-function materials

Loukia-Pantzechroula Merkouri,<sup>a</sup> Maila Danielis,<sup>id</sup><sup>b</sup> Andrea Braga,<sup>id</sup><sup>b</sup> Tomas Ramirez Reina,<sup>c</sup> Alessandro Trovarelli,<sup>b</sup> Sara Colussi<sup>id</sup><sup>b</sup>\* and Melis S. Duyar<sup>id</sup><sup>a</sup>

### Sustainability spotlight

Carbon capture, utilisation, and storage (CCUS) presents itself as a necessary part of the solution to achieve net-zero  $\text{CO}_2$  emissions by 2050. CCU entails the capture of  $\text{CO}_2$ , its compression/transportation, and its conversion into fuels and chemicals. By integrating the capture and utilisation steps, more efficient technologies are developed with reduced cost and energy requirements. Therefore, we investigate a cyclic process with two greenhouse gases ( $\text{CO}_2$ – $\text{CH}_4$ ) being introduced to our system separately, producing synthesis gas ( $\text{CO}$ – $\text{H}_2$ ). We also propose a further sustainable advancement of the technology by using green, mechanochemical synthesis, where the elimination of solvents allows for energy and waste reduction. Our work aligns with the UN sustainable development goals of affordable and clean energy (Goal 7), responsible consumption and production industry (Goal 12), and climate action (Goal 13).

obtained ratio is typically below 1 during steady-state operation due to the simultaneous occurrence of the reverse water-gas shift (RWGS) reaction (eqn (2)).<sup>12,16,17</sup> Possible side reactions apart from RWGS include  $\text{CH}_4$  cracking (eqn (3)) and Boudouard reaction (eqn (4)), both resulting in catalyst deactivation due to carbon depositions.<sup>14</sup> Typical catalysts for DRM include Ni, Co, and noble metals (*e.g.* Ru, Rh).<sup>18–26</sup>



Recently, the integrated  $\text{CO}_2$  capture and DRM (ICC-DRM) has been proposed as a  $\text{CO}_2$  mitigation technology.<sup>27,28</sup> By combining the  $\text{CO}_2$  capture and DRM processes, two harmful greenhouse gases are utilised, and the overall process efficiency is increased because the compression and transportation of both  $\text{CO}_2$  and  $\text{CH}_4$  are eliminated.<sup>4,28,29</sup> ICC-DRM involves the

<sup>a</sup>School of Chemistry and Chemical Engineering, University of Surrey, Guildford GU2 7XH, UK. E-mail: m.duyar@surrey.ac.uk

<sup>b</sup>Dipartimento Politecnico, Università degli Studi di Udine, Via del Cotonificio 108, 33100 Udine, Italy. E-mail: sara.colussi@uniud.it

<sup>c</sup>Department of Inorganic Chemistry and Materials Sciences Institute, University of Seville-CSIC, 41092 Seville, Spain



capture of CO<sub>2</sub> from a CO<sub>2</sub>-containing stream, targeting CO<sub>2</sub> upgrading in a subsequent DRM reaction. ICC-DRM resembles the typical chemical looping reforming process, but their main difference is the employment of a CO<sub>2</sub>-containing stream instead of air. As a result, there are various names for the same process in literature, such as ICC-DRM, chemical looping CH<sub>4</sub> conversion with separated CO<sub>2</sub> utilisation, and chemical (or calcium when Ca is used) looping/reforming and DRM.<sup>27,28,30</sup>

In order for the ICC-DRM to work, the material selected needs to be able to both capture the CO<sub>2</sub> from a waste stream and convert it into syngas by using CH<sub>4</sub>. This type of material is known as a dual-function material (DFM). DFMs consist of an adsorbent, such as calcium oxide (CaO) or sodium oxide (Na<sub>2</sub>O), and a catalytic active phase, such as Ni, Ru, and Rh, which are co-dispersed onto a high surface support (e.g. Al<sub>2</sub>O<sub>3</sub>). To date, DFMs have been used for other reactions, such as the CO<sub>2</sub> methanation and RWGS,<sup>4,31–37</sup> but their development in DRM is still in early stages.<sup>29,38–53</sup>

Regarding the DFMs synthesis method, the most widely used is impregnation, followed by sol gel method.<sup>4,32–34,54–58</sup> However, the solvent-free mechanochemical synthesis, where solid precursors are appropriately mixed in a ball-mill to generate the desired material,<sup>59–61</sup> can be a more sustainable method than the currently employed wet-based ones because of the reduced solvent needs and faster preparation times (hours *vs.* days), resulting in decreased energy requirements (less thermal treatments required), waste generation (solvents), and costs.<sup>60</sup> These advantages stem from the removal of solvents from the synthesis procedure, and cover many of the suggested principles of green chemistry.<sup>61</sup> The metallic dispersion is achieved by mechanical energy, bypassing the chemical and thermal equilibria involved in wet-based syntheses, producing dispersed metal catalysts that exhibit an improved performance in various reactions,<sup>61–67</sup> including conventional DRM.<sup>26,68</sup> In our previous work,<sup>61</sup> we investigated the performance of mechanochemically synthesised DFMs for the first time. Those milled DFMs had Ni and Ru nanoparticles as the catalytic phase, either Na<sub>2</sub>O or CaO as the adsorbent, and CeO<sub>2</sub>–Al<sub>2</sub>O<sub>3</sub> as the support, and they were tested in the CO<sub>2</sub> capture–RWGS process. The milling process resulted in improved dispersion of Ni, Ru and Ca when co-milled and calcined in a single step,<sup>61</sup> surpassing conventionally prepared DFMs with comparable composition<sup>41</sup> and, remarkably, despite an observed decrease in surface area. However, a distinct increase in H<sub>2</sub> reactivity was also observed, leading to a large amount of CO release during the CO<sub>2</sub> capture. Herein we exploit their higher reducibility observed in RWGS compared to wet-impregnated samples in the DRM reaction. This work is the first time that DFM materials were synthesised mechanochemically and were tested in the ICC-DRM process. By expanding on our previous work, we show that it is feasible to use milled DFMs in ICC-DRM, a more challenging process which allows the upgrading of two greenhouse gases.

## Experimental

### Materials synthesis

All the samples of this work were prepared by the dry milling method, as reported elsewhere,<sup>61</sup> and their composition was

chosen so as to be comparable of that of wet impregnated samples.<sup>41,69</sup> A Fritsch Pulverisette 23 Mini-mill was used with a 15 mL ZrO<sub>2</sub> jar and 1 ZrO<sub>2</sub> sphere (diameter: 15 mm, weight: 10 g). All the precursors were milled at 15 Hz for 20 min.<sup>61,70</sup> The support used was a commercial CeO<sub>2</sub>–Al<sub>2</sub>O<sub>3</sub> support from Sasol (SCFa-160 Ce20 Puralox, 20% CeO<sub>2</sub>). The adsorbent salt used was either Ca(NO<sub>3</sub>)<sub>2</sub> or NaNO<sub>3</sub> (both from Sigma-Aldrich), in order to ensure thermal decomposition at 600 °C while also maintaining a fair comparison with the wet impregnated references,<sup>41</sup> and the adsorbent loading was 10 wt% of the final DFM formulation. All the DFMs had 15 wt% Ni and 1 wt% Ru, and the precursors were either metallic nanopowders (Ru black from Strem Chemicals and Ni nanopowders from Sigma-Aldrich) or acetate salts (Ru(III) acetylacetone and Ni acetate, both from Sigma-Aldrich). Indeed, for the active metals, metallic nanopowders and organic precursors showed the best properties in the milling synthesis,<sup>70,71</sup> due to their non hygroscopic nature and minimum hardness compared to nitrates and metal oxides, respectively.<sup>72,73</sup> In addition, better dispersion values could be achieved.<sup>71,72</sup> We prepared nine (9) samples in total, which are shown in Table 1. First the support (CA) was co-milled with the adsorbent precursor, followed by a calcination at 600 °C for 1 h in static air, forming the supported adsorbents. After that, either the metallic nanopowders or acetate salts were milled with the supported adsorbents, and a second calcination step took place at 600 °C for 1 h. The calcination steps were carried out to remove the organic ligands and to obtain comparable materials as the wet-impregnated DFMs. Two (2) more DFMs were prepared with either Na<sub>2</sub>O or CaO and a single calcination step after the acetate precursors had been added. Finally, a reference catalyst was synthesised by using the metallic nanopowders without any adsorbent. A flowchart summarising the synthesis process is reported in the SI (Fig. S1).

### Activity tests in ICC-DRM

The cyclic CO<sub>2</sub> capture-DRM experiments of the milled samples were carried out in a tubular fixed bed quartz reactor (0.5 in OD), and the samples were placed on top of a quartz wool bed.<sup>41,61,74</sup> The outlet gas stream was analysed by an ABB AO2020 online gas analyser, after it had passed through a H<sub>2</sub>O condenser. The outlet volumetric percentages of CO<sub>2</sub>, CO, CH<sub>4</sub>, and H<sub>2</sub> were recorded every 5 s with the remaining percentage being attributed to N<sub>2</sub>. The accurate measurement of the total outlet volumetric flow rate was achieved by a bubble meter. Since N<sub>2</sub> was used as an internal standard,<sup>41,74</sup> its flow rate was not changed throughout the experiment (45 mL min<sup>−1</sup>). Initially, 0.250 g of sample was reduced at 800 °C for 1 h (10 °C min<sup>−1</sup>) by using 50 mL min<sup>−1</sup> of a 10% H<sub>2</sub>/N<sub>2</sub> mixture. Then, the temperature was decreased to 650 °C in N<sub>2</sub>, and 5 cycles of CO<sub>2</sub> capture-DRM took place. Each CO<sub>2</sub> step lasted 5 min, and each CH<sub>4</sub> step lasted 3 min. The total flow rate in both steps was 50 mL min<sup>−1</sup>, and the gaseous mixtures used were either 10% CO<sub>2</sub>/N<sub>2</sub> or 10% CH<sub>4</sub>/N<sub>2</sub>. A N<sub>2</sub> purge step was performed after each step to ensure zero readings of the gases, demonstrating that the produced gases were formed from the captured CO<sub>2</sub>.



Table 1 List of samples and brief description of synthesis parameters

#	Sample	Catalyst precursor	Calcination step (temperature, time)	# of calcination steps	Milling parameters (frequency, time)	# of milling steps
1	RuNi(M)/CaO/CA	Metallic nanopowders	600 °C/1 h	2	15 Hz/20 min	2
2	RuNi(Ac)/CaO/CA	Acetate salts	600 °C/1 h	2	15 Hz/20 min	2
3	RuNi(Ac) + CaO/CA	Acetate salts	600 °C/1 h	1	15 Hz/20 min	1
4	RuNi(M)/Na <sub>2</sub> O/CA	Metallic nanopowders	600 °C/1 h	2	15 Hz/20 min	2
5	RuNi(Ac)/Na <sub>2</sub> O/CA	Acetate salts	600 °C/1 h	2	15 Hz/20 min	2
6	RuNi(Ac) + Na <sub>2</sub> O/CA	Acetate salts	600 °C/1 h	1	15 Hz/20 min	1
7	CaO/CA	N/A	600 °C/1 h	1	15 Hz/20 min	1
8	Na <sub>2</sub> O/CA	N/A	600 °C/1 h	1	15 Hz/20 min	1
9	RuNi(M)/CA	Metallic nanopowders	600 °C/1 h	1	15 Hz/20 min	1

The N<sub>2</sub> purge after the CO<sub>2</sub> step was 10 min, and the N<sub>2</sub> purge after the CH<sub>4</sub> step was 15 min. The duration of the N<sub>2</sub> purge steps was exactly the same for all the materials tested in this work.

It should be mentioned that the purpose of having a very short CH<sub>4</sub> step was to limit the CH<sub>4</sub> cracking reaction by attempting to pulse a small amount of CH<sub>4</sub>, which was rendered impossible in the end due to our reactor setup and mass flow controllers. The DFM were tested for only 5 cycles in order to avoid the rig running overnight. The following equations (eqn (5) and (6)) were used for the calculation of the carbon balance and the residual carbon, respectively. It should be noted that the amount of H<sub>2</sub> formed due to CH<sub>4</sub> cracking was calculated by subtracting the amount of H<sub>2</sub> formed due to the DRM reaction (by assuming it was equal to the amount of CO, eqn (4)) from the total amount of H<sub>2</sub> formed in the CH<sub>4</sub> step.

Carbon balance :

$$100 \times \frac{\text{CO formed in the subsequent CO}_2 \text{ capture step}}{\text{H}_2 \text{ formed in the CH}_4 \text{ step from CH}_4 \text{ cracking}} \quad (5)$$

Residual carbon :

$$\begin{aligned} & \text{C from CH}_4 \text{ cracking} - \text{C from reverse Boudouard} \\ &= \frac{1}{2} \times \text{H}_2 \text{ formed in the CH}_4 \text{ step from CH}_4 \text{ cracking} \quad (6) \\ & - \frac{1}{2} \times \text{CO formed in the subsequent CO}_2 \text{ capture step} \end{aligned}$$

The post activity test samples were characterised by XRD. An X'Pert Powder apparatus from PANalytical was used, and the diffraction patterns were collected at 30 mA and 40 kV by using Cu K $\alpha$  radiation ( $\lambda = 1.5406 \text{ \AA}$ ) while the  $2\theta$  angle was increased every 450 s by  $0.05^\circ$  in the range of  $10\text{--}90^\circ$ . The average Ni crystalline size was estimated by the Scherrer's equation at  $44.5^\circ$  (Ni(111) phase).

## Results and discussion

The performance of all samples, *i.e.* the DFMs, the supported adsorbents, and the catalyst, was evaluated in ICC-DRM. Fig. 1 shows the quantities of products, CO and H<sub>2</sub>, and the H<sub>2</sub>/CO ratio during the CH<sub>4</sub> steps. A comparison with similar samples

prepared by conventional methods is reported in Table S1. By observing Fig. 1a, it was made clear that all 9 samples, including the supported adsorbents and the catalyst, were active in ICC-DRM. That meant that they were able to capture the CO<sub>2</sub> during the CO<sub>2</sub> steps and then convert it into syngas *via* the DRM reaction. The most active sample was by far sample 3 (RuNi(Ac) + CaO/CA), which produced  $588 \text{ }\mu\text{mol g}^{-1}$  of CO on average during the CH<sub>4</sub> steps. This sample achieved a high degree of interaction between the DFM components and a good dispersion of both the catalyst and the adsorbent through the dry milling of Ca with the acetate precursors, followed by a single calcination step, as characterised *via* scanning transmission electron microscopy results in our previous publication.<sup>61</sup> The amount of CO formed during the CH<sub>4</sub> steps seemed to be fairly stable over the cycles for all samples, and the order of DFMs according to their average CO production in CH<sub>4</sub> steps was: sample 3 ( $588 \text{ }\mu\text{mol g}^{-1}$ ) > sample 1 ( $295 \text{ }\mu\text{mol g}^{-1}$ ) > sample 2 ( $257 \text{ }\mu\text{mol g}^{-1}$ ) > sample 5 ( $200 \text{ }\mu\text{mol g}^{-1}$ ) > sample 6 ( $194 \text{ }\mu\text{mol g}^{-1}$ ) > sample 9 ( $181 \text{ }\mu\text{mol g}^{-1}$ ) > sample 4 ( $174 \text{ }\mu\text{mol g}^{-1}$ ) > sample 7 ( $67 \text{ }\mu\text{mol g}^{-1}$ ) > sample 8 ( $62 \text{ }\mu\text{mol g}^{-1}$ ).

Fig. 1b displays the amount of H<sub>2</sub> produced during the CH<sub>4</sub> steps, which was much higher than the amount of CO for all samples. From Fig. 1c, it was clear that the H<sub>2</sub>/CO was much higher than the stoichiometric value, with the highest H<sub>2</sub>/CO observed for sample 2, *i.e.* 21.3. This indicated that a side reaction took place, namely the CH<sub>4</sub> cracking reaction (eqn (3)). Once the adsorbed CO<sub>2</sub> had been consumed, the high temperature used in these experiments ( $650^\circ\text{C}$ ) allowed the endothermic CH<sub>4</sub> cracking reaction to take place, producing an excess amount of H<sub>2</sub>. Interestingly, the amount of H<sub>2</sub> produced decreased over the cycles except for the supported adsorbents (samples 7 and 8). That indicated that the extent of CH<sub>4</sub> cracking was reduced over time, meaning that the surface of DFMs was not 'clean' of carbon depositions, which in turn hindered the CH<sub>4</sub> cracking reaction over the cycles. The order of samples according to their average H<sub>2</sub> production in CH<sub>4</sub> steps was: sample 3 ( $7697 \text{ }\mu\text{mol g}^{-1}$ ) > sample 2 ( $5504 \text{ }\mu\text{mol g}^{-1}$ ) > sample 5 ( $3455 \text{ }\mu\text{mol g}^{-1}$ ) > sample 6 ( $3042 \text{ }\mu\text{mol g}^{-1}$ ) > sample 1 ( $2773 \text{ }\mu\text{mol g}^{-1}$ ) > sample 9 ( $2677 \text{ }\mu\text{mol g}^{-1}$ ) > sample 4 ( $1847 \text{ }\mu\text{mol g}^{-1}$ ) > sample 7 ( $798 \text{ }\mu\text{mol g}^{-1}$ ) > sample 8 ( $776 \text{ }\mu\text{mol g}^{-1}$ ). This order was the same as the order of the CO production with the only difference being sample 1, which dropped to the 5th place, explaining why it had the lowest H<sub>2</sub>/CO in Fig. 1c.



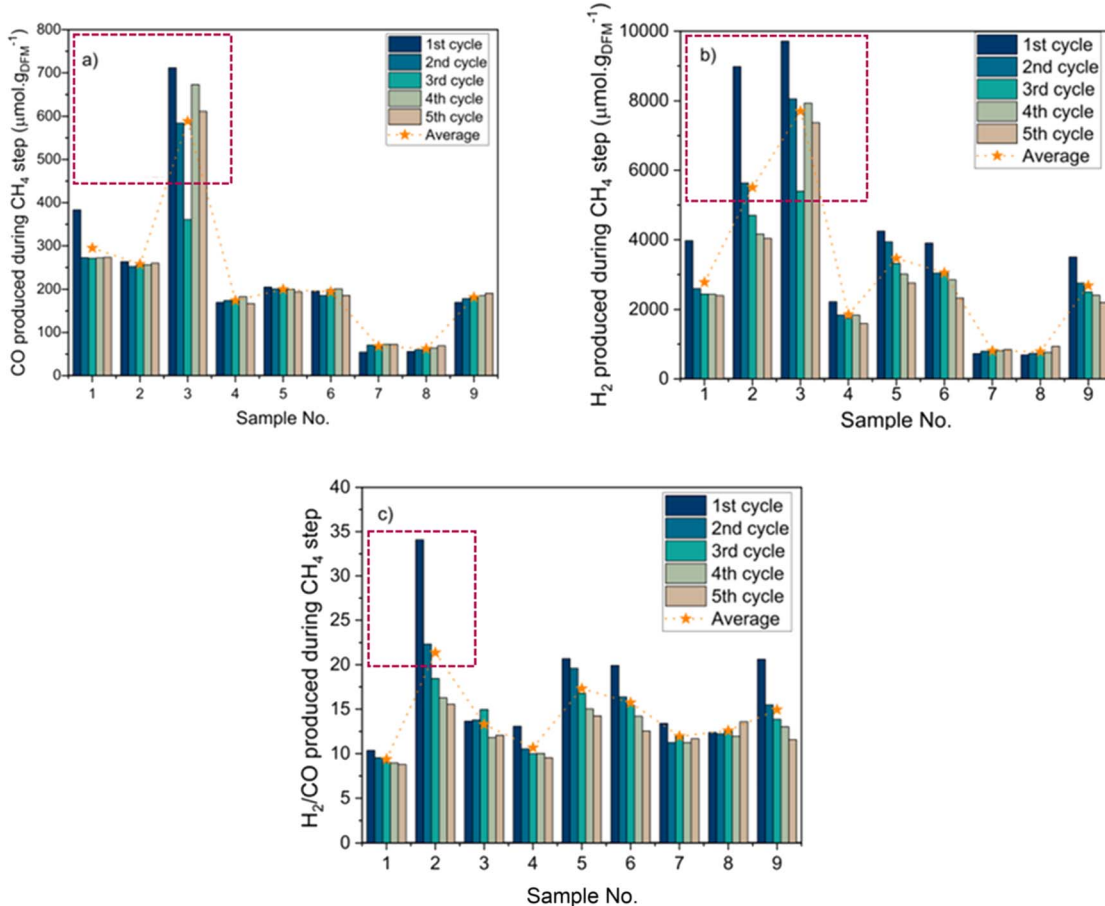


**Fig. 1** Amount of (a) CO and (b) H<sub>2</sub> formed, and corresponding (c) H<sub>2</sub>/CO ratio measured during the CH<sub>4</sub> steps. (1) RuNi(M)/CaO/CA; (2) RuNi(Ac)/CaO/CA; (3) RuNi(Ac) + CaO/CA; (4) RuNi(M)/Na<sub>2</sub>O/CA; (5) RuNi(Ac)/Na<sub>2</sub>O/CA; (6) RuNi(Ac) + Na<sub>2</sub>O/CA; (7) CaO/CA; (8) Na<sub>2</sub>O/CA; (9) RuNi(M)/CA. The red dashed square indicates the best performing samples.

Overall, the Ca-containing DFMs exhibited the best ICC-DRM performance, which was expected because Ca is more efficient in capturing CO<sub>2</sub> at higher temperatures than Na due to its higher amount of medium-strong basic sites.<sup>41,75,76</sup> In our case, Ca was expected to have formed more stable carbonates compared with Na and so, less amount of weakly CO<sub>2</sub> was desorbed during the N<sub>2</sub> purge steps, leading to higher reforming efficiency.<sup>28,34,75-79</sup> The supported adsorbents had the worst performance because they did not have Ni or Ru in their formulation to boost the conversion of the adsorbed CO<sub>2</sub> into syngas. After all, Ni and Ru are perhaps the most active and widely used metals for the DRM reaction.<sup>12-15,80,81</sup> In contrast, the opposite trend was observed during their CO<sub>2</sub> capture-RWGS experiments<sup>61</sup> as the supported adsorbents were the most active samples after sample 3, suggesting that RWGS mainly took place due to the adsorbent and/or CeO<sub>2</sub>. In the ICC-DRM case, the supported adsorbents did produce some amounts of CO and H<sub>2</sub> because of the adsorbent itself and the ability of CeO<sub>2</sub> to help catalyse the DRM reaction,<sup>21,82-86</sup> but not as large CO and H<sub>2</sub> quantities as the DFMs due to the lack of the active metal phase. The reference catalyst was also able to produce syngas. Ni and Ru had the ability to adsorb CO<sub>2</sub> and form carbonyl species, which were converted into CO and H<sub>2</sub>

during the CH<sub>4</sub> steps.<sup>87-92</sup> In fact, the amount of CO produced by the catalyst was similar to the amount of CO produced by the Na-containing DFMs, while the catalyst (sample 9) outperformed sample 4 in both CO and H<sub>2</sub> production too. By comparing sample 1 (RuNi(M)/CaO/CA), sample 4 (RuNi(M)/Na<sub>2</sub>O/CA), and sample 9 (RuNi(M)/CA), it was deduced that only the Ca adsorbent enhanced the ICC-DRM performance and so, Na was not a good adsorbent at the selected temperature (650 °C).<sup>79</sup> Hence, a synergy between the Ca adsorbent, support, and NiRu is necessary for successful ICC-DRM applications, where Ca efficiently binds CO<sub>2</sub><sup>76</sup> which is then made available to close Ni and Ru sites<sup>61</sup> for CH<sub>4</sub> reforming to syngas. Opposite trends regarding the number of calcination steps were observed for the two sorbent elements. As regards the Na-containing DFMs, sample 5 (2 calcination steps) was marginally more active than sample 6 (1 calcination step). On the other hand, regarding the Ca-containing DFMs, sample 3 (1 calcination step) was more active than sample 2 (2 calcinations steps), likely due to the improved Ca-Ni-Ru proximity induced by the milling synthesis.<sup>61</sup>

By comparing the type of precursor used, the acetate precursor (sample 5) was better than the metallic nanopowders (sample 4) when Na was used as an adsorbent. The results

varied for the Ca-containing DFM samples (samples 1 and 2). Even though sample 1 (RuNi(M)/CaO/CA) produced more CO than sample 2 (RuNi(Ac)/CaO/CA), the opposite was true for the H<sub>2</sub> production. It clearly showed that sample 2 was more susceptible to CH<sub>4</sub> cracking reaction compared to sample 1, as seen in Fig. 1c.

Fig. 2 illustrates the CO and H<sub>2</sub> volumetric flow rates of the most active Ca-containing (sample 3) and Na-containing (sample 5) samples, and the remaining samples are shown in Fig. S2. Both samples produced a much larger amount of H<sub>2</sub> than CO during the CH<sub>4</sub> steps, as Fig. 1 showed. It seemed that the DFM samples produced a high quantity of H<sub>2</sub> during the CH<sub>4</sub> steps and a high quantity of CO during the CO<sub>2</sub> steps, apart from the first CO<sub>2</sub> step. The small amount of CO during the first CO<sub>2</sub> step was attributed to the occurrence of the RWGS reaction between the available CO<sub>2</sub> and the chemisorbed H<sub>2</sub>.<sup>41,61</sup> It was also considered possible that the CO production happened because of CO<sub>2</sub> dissociation on highly reduced Ru, Ni, and CeO<sub>2</sub> sites.<sup>61</sup> Larger amounts of CO were formed during the first CO<sub>2</sub> step of the Ca-containing DFM samples (samples 1–3) compared to the Na-containing DFM samples (samples 4–6) with an average CO production of 95 and 32  $\mu\text{mol g}^{-1}$ , respectively, as Fig. S2 illustrates. Interestingly, the supported adsorbents and the catalyst (samples 7–9) produced a small amount of CO, *ca.* 11  $\mu\text{mol g}^{-1}$ , indicating that Ce<sup>3+</sup> was oxidised by CO<sub>2</sub>, forming CO and Ce<sup>4+</sup> and confirming our CO<sub>2</sub> dissociation hypothesis stated earlier. Ceria is well-known for its excellent redox properties, its increased oxygen vacancies, and its ability to catalyse the RWGS reaction.<sup>93–98</sup> The formation of CO due to the decomposition of formate species (HCOO<sup>−</sup>) into CO and OH was not considered in this case, because DRIFTS studies of the corresponding wet-impregnated samples did not show the formation of formate species.<sup>87,88</sup> Future DRIFTS experiments can be carried out to investigate the reaction mechanism of those DFM samples, but those experiments are out of the scope of this work. Additionally, some amounts of H<sub>2</sub> were observed in every CO<sub>2</sub> capture step, indicating that H<sub>2</sub> was chemisorbed on the surface due to the

initial DFM reduction or CH<sub>4</sub> cracking and that it was then released upon a CO<sub>2</sub> flow.

The significant amounts of CO produced in the CO<sub>2</sub> steps indicated the gasification of carbon through the reverse Boudouard reaction (reverse eqn (4)). In effect, CO<sub>2</sub> reacted with the carbon formed in the preceding CH<sub>4</sub> step, producing substantial amounts of CO. Despite the production of excess H<sub>2</sub> in the CH<sub>4</sub> steps, it was observed that the onset of CO was at the same time as H<sub>2</sub>, or perhaps few seconds before that, and that CO had stopped being produced after the first 5 min. In other words, DRM took place before CH<sub>4</sub> cracking, and as the time went by and the availability of adsorbed CO<sub>2</sub> decreased, CH<sub>4</sub> cracking became the dominant reaction. Even though the CH<sub>4</sub> flow lasted only 3 min, it took a considerable amount of time to purge the leftover CH<sub>4</sub> of the lines, and as long as CH<sub>4</sub> was still present, it continued to decompose into carbon and H<sub>2</sub>. That meant that even though the CH<sub>4</sub> step lasted only 3 min and no CH<sub>4</sub> flowed after that time, CH<sub>4</sub> cracking continued to occur during the subsequent N<sub>2</sub> purge step, and it finished when there was no CH<sub>4</sub> left in the lines. Since H<sub>2</sub> was present in the CH<sub>4</sub> step, the simultaneous occurrence of RWGS during the CH<sub>4</sub> steps could not be ruled out completely since those DFM samples have shown to be active in that reaction.<sup>61</sup> It should be noted that CO<sub>2</sub> was not desorbed during the CH<sub>4</sub> steps in any of the samples apart from the most active sample (sample 3). However, its amount was so small ( $\ll 10 \mu\text{mol g}^{-1}$ ) that could not be accurately quantified and so, it was concluded that DRM was a fast reaction and that all the adsorbed CO<sub>2</sub> had been converted into syngas.

Fig. 3 shows the amount of CO formed during the CO<sub>2</sub> steps and the residual amount of carbon left on the surface after each CO<sub>2</sub> step. Since the first step after the reduction of the DFM samples was a CO<sub>2</sub> capture step and CH<sub>4</sub> had not been introduced to the reactor beforehand, there was only a very small amount of CO formed during the first CO<sub>2</sub> capture step. In addition, Fig. 3a reveals that the supported adsorbents produced minimal amounts of CO through the reverse Boudouard reaction and so, this reaction occurred due to the presence of Ni and Ru. Similar

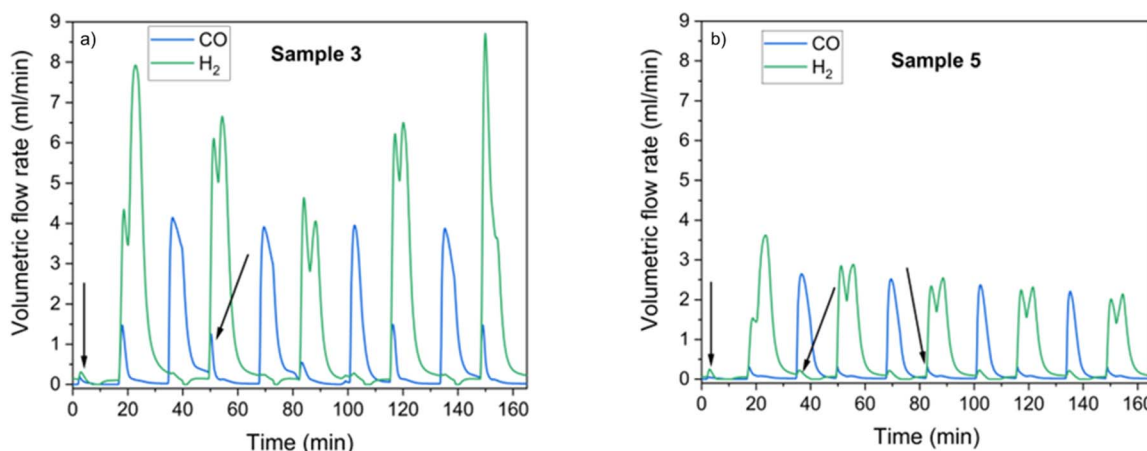


Fig. 2 Volumetric flow rate of CO and H<sub>2</sub> vs. time graphs of the best performing (a) Ca-containing DFM (sample 3: RuNi(Ac) + CaO/CA) and (b) Na-containing DFM (sample 5: RuNi(Ac)/Na<sub>2</sub>O/CA).



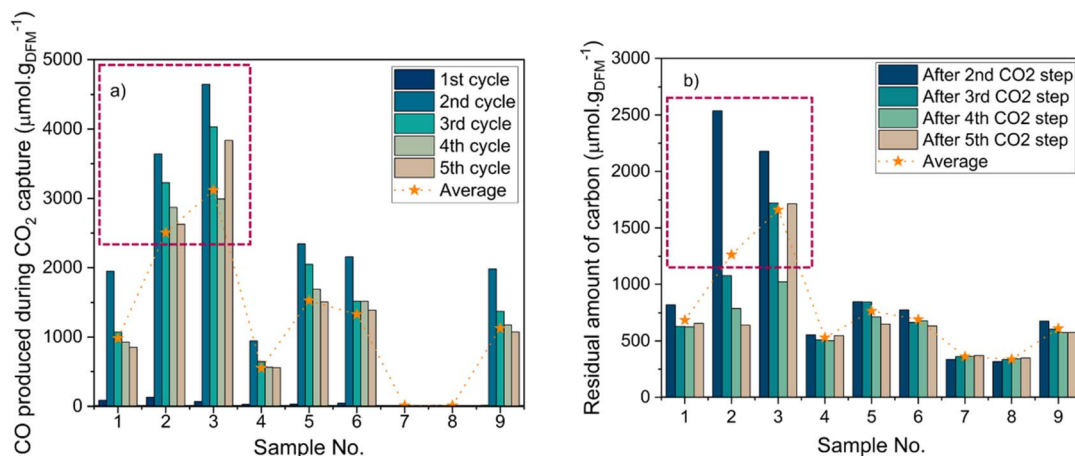


Fig. 3 (a) Amount of CO formed during the CO<sub>2</sub> steps and (b) amount of residual carbon (found by subtracting the carbon gasified in the subsequent CO<sub>2</sub> capture step from the carbon formed due to CH<sub>4</sub> cracking in the previous cycle). (1) RuNi(M)/CaO/CA; (2) RuNi(Ac)/CaO/CA; (3) RuNi(Ac) + CaO/CA; (4) RuNi(M)/Na<sub>2</sub>O/CA; (5) RuNi(Ac)/Na<sub>2</sub>O/CA; (6) RuNi(Ac) + Na<sub>2</sub>O/CA; (7) CaO/CA; (8) Na<sub>2</sub>O/CA; (9) RuNi(M)/CA. The red dashed square indicates the best performing samples.

to the amount of H<sub>2</sub> formed during the CH<sub>4</sub> steps (Fig. 1b), the amount of CO during the CO<sub>2</sub> steps decreased over the cycles, meaning that the extent of CH<sub>4</sub> cracking decreased over time. The order of samples based on the average amount of CO produced during the CO<sub>2</sub> steps was: sample 3 (3116 μmol g<sup>-1</sup>) > sample 2 (2499 μmol g<sup>-1</sup>) > sample 5 (1523 μmol g<sup>-1</sup>) > sample 6 (1325 μmol g<sup>-1</sup>) > sample 9 (1122 μmol g<sup>-1</sup>) > sample 1 (976 μmol g<sup>-1</sup>) > sample 4 (547 μmol g<sup>-1</sup>) > sample 7 (4 μmol g<sup>-1</sup>) > sample 8 (4 μmol g<sup>-1</sup>). That order was the same as the H<sub>2</sub> production order with the only difference being the change of order between samples 1 and 9.

As both the production of H<sub>2</sub> from CH<sub>4</sub> cracking and CO from reverse Boudouard decreased over time, the amount of residual carbon remained somewhat stable (samples 1, 4, 7 and 8) or decreased over time (samples 2, 3, 5, 6 and 9), as illustrated in Fig. 3b. Based on Table S2, the carbon balance was not closed in any of the samples, likely due to a continuous accumulation of the carbon species from CH<sub>4</sub> cracking. Despite the gasification of carbon in the subsequent CO<sub>2</sub> capture step, it was not enough to get rid of the carbon completely. Apparently, the most active samples in ICC-DRM had the highest amount of residual carbon left. Since the amount of CO formed during the CH<sub>4</sub> steps (Fig. 1a) was stable over time, it was shown that the carbon accumulation did not affect the DRM activity of the designed DFMs. This was a significant result, but experiments with a duration of few days will be necessary in the future to observe their behaviour over longer periods of time. Carbon deposition, *i.e.* coking, is usually a well-known deactivation mechanism. The possibility of gasifying the carbon *via* the reverse Boudouard reaction, as demonstrated in this work, creates new opportunities for materials regeneration. Further material optimisation, for example by reducing Ni loading,<sup>99</sup> can also be explored to limit CH<sub>4</sub> cracking and the consequent carbon deposition. The DFM that had the most-closed carbon balance was sample 2 with an average carbon balance of 58%, followed by sample 5 (55%), samples 3 and 6 (54%), sample

(45%), and sample 4 (39%). This trend confirmed that the DFMs synthesised with acetate precursors were better than the ones with metallic nanopowders (Fig. 1). It is worth mentioning that the accurate quantification of carbon deposition by characterising the post samples was not feasible in this case. That was due to the complexity of the designed materials and the interference of carbonate decomposition, material oxidation, RuO<sub>x</sub> volatility, and chemisorbed/adsorbed species (*e.g.* H<sub>2</sub>O) with the carbon deposition analysis.

Fig. S3 and Table S3 show the post XRD patterns and estimated Ni particle sizes based on the Scherrer equation. The post XRD patterns were very similar to their *ex situ* reduced pattern, observed in our previous work.<sup>61</sup> All samples presented the characteristic peaks of CeO<sub>2</sub> and γ-Al<sub>2</sub>O<sub>3</sub> (JCPDS 03-065-5923 and JCPDS 00-004-0880, respectively). The DFMs also had metallic Ni peaks (JCPDS 01-070-1849). None of the samples showed any phase of Ru or the adsorbent (Ca/Na), meaning that those species were highly dispersed and/or amorphous. Despite the last step being a CH<sub>4</sub> step, no crystalline carbon peak was observed and so, the accumulated carbon was not graphitic, but soft/amorphous, facilitating possible regeneration pathways. Based on Table S3, the average crystalline size of Ni increased by 1–2 nm in the Na-containing DFMs (samples 4–6) and reference catalyst (sample 9) compared to their corresponding reduced samples. In the case of the Ca-containing DFMs (samples 1–3), it increased by *ca.* 5 nm. It could be concluded that the Ca-containing DFMs were more prone to sintering than the Na-containing DFMs. Since they were also the most active samples in the ICC-DRM, it was demonstrated that the formation of carbon depositions enhanced the metallic sintering to some extent in fair agreement with previous reports.<sup>100,101</sup> However, the increase was not that significant, and the main culprit in our materials for the ICC-DRM process remained the carbon formation and accumulation, making necessary the implementation of a regeneration process and/or an optimisation of the DFM to suppress CH<sub>4</sub> cracking.

## Conclusions

In this work, we used mechanochemically milled DFM for the first time in ICC-DRM, demonstrating the feasibility of the dry milling synthesis method for this process. The six (6) milled DFM investigated herein differed in the adsorbent (Na or Ca), the type of catalyst precursor (metallic nanopowders or acetate), and the number of calcination steps (1 or 2). The most active DFM was sample 3 that had Ca as an adsorbent and was synthesised by using acetate precursors and a single calcination step. In general, using Ca as an adsorbent and acetates as a catalyst precursor resulted in the best materials, due to the high temperature favouring calcium carbonates formation and the ease of dispersion allowed by Ni and Ru acetates. However, all samples tested, including the two supported adsorbents and the reference catalyst, produced CO and excess amounts of H<sub>2</sub> during the CH<sub>4</sub> steps, leading to a H<sub>2</sub>/CO of more than 10. Even though DRM took place between the captured CO<sub>2</sub> and the available CH<sub>4</sub>, significant quantities of H<sub>2</sub> were produced due to CH<sub>4</sub> cracking. As a result, carbon was formed and accumulated over time, only partially gasified in the subsequent CO<sub>2</sub> capture step through the reverse Boudouard reaction, releasing large amounts of CO. However, none of the samples had a closed carbon balance. Despite the carbon formation, the activity of DFM in DRM was steady over the five cycles, allowing us to preliminarily validate the implementation of multicomponent DFM systems prepared by milling for ICC-DRM as a smart strategy for chemical CO<sub>2</sub> recycling. The use of a solvent-free synthesis method has distinct advantages in terms of materials costs and waste reduction, directly correlated with the solvent use reduction, a consequent decrease in thermal treatment requirements, hence leading to energy and time savings. Additionally, a more facile scalability of this technology can be envisioned compared to other methods, such as sol-gel or combustion syntheses, since large-scale milling is already employed in other industrial processes while the sol-gel and combustion alternatives are difficult to reproduce and represent a safety problem at industry level. Another advantage of the milling method is the facilitation of fast material screening, that can be exploited for example to investigate the optimal Ni loading to balance high DRM activity with low CH<sub>4</sub> cracking and, consequently, low carbon deposition. Thus, a sample with optimal Ni loading might not require complex regeneration protocols, overcoming the issues observed so far. Nevertheless, further optimisation studies will likely be needed in the future aiming to minimise the carbon formation; this should include fine-tuning the DFM composition (*e.g.* reducing metal content) and process conditions (*e.g.* reaction temperature and duration) as well as engineering a viable regeneration protocol (*e.g.* by using either hydrogen or air) to unlock the potential of DFM for realistic ICC-DRM applications.

## Author contributions

Loukia-Pantzechroula Merkouri: methodology, investigation, formal analysis, visualisation, writing – original draft. Maila Daniellis: methodology, investigation, formal analysis, writing – review

and editing. Andrea Braga: investigation, formal analysis, writing – review and editing. Tomas Ramirez Reina: formal analysis, writing – review and editing. Alessandro Trovarelli: supervision, resources. Sara Colussi: conceptualisation, writing – review and editing, supervision, resources. Melis S. Duyar: conceptualisation, formal analysis, writing – review and editing, supervision, funding acquisition, resources, project administration.

## Conflicts of interest

There are no conflicts to declare.

## Data availability

Data supporting this article have been included as part of the SI.

Supplementary information including details of material synthesis, further characterization and time dependent data from DFM activity tests. See DOI: <https://doi.org/10.1039/d5su00317b>.

## Acknowledgements

This study was carried out within the Interconnected Nord-Est Innovation Ecosystem (iNEST) and received funding from the European Union Next-GenerationEU (PIANO NAZIONALE DI RIPRESA E RESILIENZA (PNRR) – MISSIONE 4 COMPONENTE 2, INVESTIMENTO 1.5 – D.D. 1058 23/06/2022, ECS00000043, CUP: G23C22001130006). M. D. is grateful for funding under the REACT EU Italian PON 2014–2020 Program – Action IV.4 – Innovation (DM 1062, 10/08/2021, CUP G51B21006040007). S. C., M. S. D. and T. R. R. acknowledge funding by the European Commission under the framework of C-NET project, HORIZON-MSCA-2023-SE-01, project reference: 101182598. M. S. D. acknowledges support by the Engineering and Physical Sciences Research Council (EPSRC) grant EP/X000753/1. Views and opinions expressed are however those of the author(s) only and do not necessarily reflect those of the European Union. Neither the European Union nor the granting authority can be held responsible for them. The team of the University of Surrey acknowledge the financial support for this work from the School of Chemistry and Chemical Engineering and the Doctoral College of the University of Surrey. SASOL is kindly acknowledged for providing the CeAl support.

## References

- United Nations Framework Convention on Climate Change, *Adoption of the Paris Agreement*, Paris, 2015.
- J. Rogelj, M. Den Elzen, N. Höhne, T. Fransen, H. Fekete, H. Winkler, R. Schaeffer, F. Sha, K. Riahi and M. Meinshausen, *Nature*, 2016, 534, 631–639.
- CO<sub>2</sub> Emissions in 2023, <https://www.iea.org/reports/co2-emissions-in-2023>, accessed 16 September 2024.
- L. P. Merkouri, T. R. Reina and M. S. Duyar, *Energy Fuels*, 2021, 35, 19859–19880.
- Global Surface Temperature|NASA Global Climate Change, *Climate Change: Vital Signs of the Planet*, <https://>



[climate.nasa.gov/vital-signs/carbon-dioxide/](https://climate.nasa.gov/vital-signs/carbon-dioxide/), accessed 16 September 2024.

6 O. Boucher, P. Friedlingstein, B. Collins and K. P. Shine, *Environ. Res. Lett.*, 2009, **4**, 044007.

7 *CO<sub>2</sub> Emissions in 2022*, <https://www.iea.org/reports/co2-emissions-in-2022>, accessed 15 March 2023.

8 J. C. M. Pires, F. G. Martins, M. C. M. Alvim-Ferraz and M. Simões, *Chem. Eng. Res. Des.*, 2011, **89**, 1446–1460.

9 A. Al-Mamoori, A. Krishnamurthy, A. A. Rownaghi and F. Rezaei, *Energy Technol.*, 2017, **5**, 834–849.

10 E. A. Quadrelli, G. Centi, J. L. Duplan and S. Perathoner, *ChemSusChem*, 2011, **4**, 1194–1215.

11 J. Gibbins and H. Chalmers, *Energy Policy*, 2008, **36**, 4317–4322.

12 E. le Saché and T. R. Reina, *Prog. Energy Combust. Sci.*, 2022, **89**, 100970.

13 B. Abdullah, N. A. Abd Ghani and D. V. N. Vo, *J. Cleaner Prod.*, 2017, **162**, 170–185.

14 S. Arora and R. Prasad, *RSC Adv.*, 2016, **6**, 108668–108688.

15 J. M. Lavoie, *Front. Chem.*, 2014, **2**, 1–17.

16 M. Usman, W. M. A. Wan Daud and H. F. Abbas, *Renewable Sustainable Energy Rev.*, 2015, **45**, 710–744.

17 F. M. Baena-Moreno, M. Rodríguez-Galán, F. Vega, B. Alonso-Fariñas, L. F. Vilches Arenas and B. Navarrete, *Energy Sources, Part A*, 2019, **41**, 1403–1433.

18 J. L. Martín-Espejo, L.-P. Merkouri, J. Gándara-loe, J. A. Odriozola, T. Ramírez Reina and L. Pastor-Pérez, *J. Environ. Sci.*, 2024, **140**, 12–23.

19 J. L. Martín-Espejo, L. P. Merkouri, J. A. Odriozola, T. Ramírez Reina and L. Pastor-Pérez, *Ceram. Int.*, 2024, **50**, 38406–38414.

20 S. A. Ali, M. Sa, L.-P. Merkouri, S. Soodi, A. Iakovidis, M. S. Duyar, D. Neagu, T. R. Reina and K. Kousi, *Front. Energy Res.*, 2023, **11**, 1–9.

21 C. A. H. Price, W. Arnold, L. Pastor-Pérez, B. Amini-Horri and T. R. Reina, *Top. Catal.*, 2020, **63**, 281–293.

22 E. le Saché, L. Pastor-Pérez, D. Watson, A. Sepúlveda-Escribano and T. R. Reina, *Appl. Catal., B*, 2018, **236**, 458–465.

23 C. A. H. Price, L. Pastor-Pérez, T. Ramírez Reina and J. Liu, *React. Chem. Eng.*, 2018, **3**, 433–436.

24 A. Álvarez Moreno, T. Ramírez-Reina, S. Ivanova, A. C. Roger, M. Á. Centeno and J. A. Odriozola, *Front. Chem.*, 2021, **9**, 1–10.

25 I. Luisetto, S. Tuti, C. Battocchio, S. Lo Mastro and A. Sodo, *Appl. Catal., A*, 2015, **500**, 12–22.

26 M. Armengol-Profitós, A. Braga, L. Pascua-Solé, I. Lucentini, X. Garcia, L. Soler, X. Vendrell, I. Serrano, I. J. Villar-Garcia, V. Pérez-Dieste, C. Escudero, N. J. Divins and J. Llorca, *Appl. Catal., B*, 2024, **345**, 123624.

27 E. Wang, Z. Zhu, R. Li, J. Wu, K. Ma and J. Zhang, *Chem. Eng. J.*, 2024, **482**, 148476.

28 A. Bhaskaran, S. A. Singh, B. M. Reddy and S. Roy, *Langmuir*, 2024, **40**, 14766–14778.

29 J. Hu, P. Hongmanorom, V. V. Galvita, Z. Li and S. Kawi, *Appl. Catal., B*, 2021, **284**, 119734.

30 Z. Zhou, Z. Sun and L. Duan, *Curr. Opin. Green Sustainable Chem.*, 2023, **39**, 100721.

31 A. Tsotsias, N. Charisiou, I. Yentekakis and M. Goula, *Chem. Proc.*, 2020, **2**, 35.

32 J. Chen, Y. Xu, P. Liao, H. Wang and H. Zhou, *Carbon Capture Sci. Technol.*, 2022, **4**, 100052.

33 K. Zhang, D. Guo, X. Wang, Y. Qin, L. Hu and Y. Zhang, *J. CO<sub>2</sub> Util.*, 2023, **72**, 102493.

34 L.-P. Merkouri, A. I. Paksoy, T. R. Reina and M. S. Duyar, *ACS Catal.*, 2023, **13**, 7230–7242.

35 A. I. Tsotsias, E. Harkou, N. D. Charisiou, V. Sebastian, D. R. Naikwadi, B. van der Linden, A. Bansode, D. Stoian, G. Manos, A. Constantinou and M. A. Goula, *J. Energy Chem.*, 2025, **102**, 309–328.

36 A. I. Tsotsias, N. D. Charisiou, A. G. S. Hussien, V. Sebastian, K. Polychronopoulou and M. A. Goula, *Chem. Eng. J.*, 2024, **491**, 151962.

37 A. I. Tsotsias, N. D. Charisiou, A. G. S. Hussien, A. A. Dabbawala, V. Sebastian, K. Polychronopoulou and M. Goula, *J. Environ. Chem. Eng.*, 2024, **12**, 112712.

38 S. Jo, J. H. Lee, J. H. Woo, T.-Y. Kim, H.-J. Ryu, B. Hwang, J. C. Kim, S. C. Lee and K. L. Gilliard-AbdulAziz, *Sustainable Energy Fuels*, 2022, **6**, 81–88.

39 M. Najimu, S. Jo and K. L. Gilliard-AbdulAziz, *Acc. Chem. Res.*, 2023, **56**, 3132–3141.

40 S. Jo, J. H. Woo, J. H. Lee, T. Y. Kim, H. I. Kang, S. C. Lee and J. C. Kim, *Sustainable Energy Fuels*, 2020, **4**, 5543–5549.

41 L.-P. Merkouri, R. Reina and M. S. Duyar, *Nanoscale*, 2022, **14**, 12620–12637.

42 S. Sun, Y. Zhang, C. Li, Y. Wang, C. Zhang, X. Zhao, H. Sun and C. Wu, *Sep. Purif. Technol.*, 2023, **308**, 122956.

43 X. Zhao, S. Sun, Y. Zhang, Y. Wang, Y. Zhu, P. Williams, S. Guan and C. Wu, *Sep. Purif. Technol.*, 2023, **326**, 124866.

44 S. Sun, C. Zhang, Y. Wang, X. Zhao, H. Sun and C. Wu, *Chem. Eng. J.*, 2023, **468**, 143712.

45 S. Sun, Y. Wang, Y. Xu, H. Sun, X. Zhao, Y. Zhang, X. Yang, X. Bie, M. Wu, C. Zhang, Y. Zhu, Y. Xu, H. Zhou and C. Wu, *Appl. Catal., B*, 2024, **348**, 123838.

46 L. Zhu, Z. Lv, X. Huang, S. Lu, J. Ran and C. Qin, *Fuel Process. Technol.*, 2023, **248**, 107838.

47 S. Jo and K. L. Gilliard-AbdulAziz, *Small*, 2024, e2401156.

48 S. M. Kim, P. M. Abdala, M. Broda, D. Hosseini, C. Copéret and C. Müller, *ACS Catal.*, 2018, **8**, 2815–2823.

49 S. Tian, F. Yan, Z. Zhang and J. Jiang, *Sci. Adv.*, 2019, **5**, eaav5077.

50 H. Gu, Y. Gao, S. Iftikhar and F. Li, *J. Mater. Chem. A*, 2022, **10**, 3077–3085.

51 R. Han, S. Xing, Y. Wang, L. Wei, Z. Li, C. Yang, C. Song and Q. Liu, *Sep. Purif. Technol.*, 2023, **307**, 122808.

52 B. Shao, Z. Q. Wang, X. Q. Gong, H. Liu, F. Qian, P. Hu and J. Hu, *Nat. Commun.*, 2023, **14**, 996.

53 D. Pinto, L. Hu and A. Urakawa, *Chem. Eng. J.*, 2023, **474**, 145641.

54 I. S. Omodolor, H. O. Otor, J. A. Andonegui, B. J. Allen and A. C. Alba-Rubio, *Ind. Eng. Chem. Res.*, 2020, **59**, 17612–17631.



55 S. Sun, H. Sun, P. T. Williams and C. Wu, *Sustainable Energy Fuels*, 2021, **5**, 4546–4559.

56 P. Melo Bravo and D. P. Debecker, *Waste Disposal Sustainable Energy*, 2019, **1**, 53–65.

57 A. I. Tsotsias, N. D. Charisiou, I. V. Yentekakis and M. A. Goula, *Catalysts*, 2020, **10**, 812.

58 W. J. Tan and P. Gunawan, *Inorganics*, 2023, **11**, 464.

59 A. Braga, M. Danielis, S. Colussi and A. Trovarelli, *RSC Mechatnochem.*, 2025, **2**, 516–528.

60 M. Danielis, S. Colussi, N. J. Divins, L. Soler, A. Trovarelli and J. Llorca, *Johnson Matthey Technol. Rev.*, 2024, **68**, 217–231.

61 M. Danielis, L. P. Merkouri, A. Braga, A. Trovarelli, M. S. Duyar and S. Colussi, *J. CO<sub>2</sub> Util.*, 2024, **86**, 102895.

62 A. P. Amrute, J. De Bellis, M. Felderhoff and F. Schüth, *Chem.-Eur. J.*, 2021, **27**, 6819–6847.

63 J. L. Do and T. Friščić, *ACS Cent. Sci.*, 2017, **3**, 13–19.

64 M. Danielis, J. D. Jiménez, N. Rui, J. Moncada, L. E. Betancourt, A. Trovarelli, J. A. Rodriguez, S. D. Senanayake and S. Colussi, *Appl. Catal., A*, 2023, **660**, 119185.

65 J. D. Jiménez, L. E. Betancourt, M. Danielis, H. Zhang, F. Zhang, I. Orozco, W. Xu, J. Llorca, P. Liu, A. Trovarelli, J. A. Rodríguez, S. Colussi and S. D. Senanayake, *ACS Catal.*, 2022, **12**, 12809–12822.

66 A. Braga, M. Armengol-Profitós, L. Pascua-Solé, X. Vendrell, L. Soler, I. Serrano, I. J. Villar-Garcia, V. Pérez-Dieste, N. J. Divins and J. Llorca, *ACS Appl. Nano Mater.*, 2023, **6**, 7173–7185.

67 Y. Huang, W. Liu, J. Y. Yong, X. J. Zhang, C. Wu and L. Jiang, *Renewable Sustainable Energy Rev.*, 2025, **208**, 115029.

68 J. D. Jiménez, L. E. Betancourt, M. Danielis, H. Zhang, F. Zhang, I. Orozco, W. Xu, J. Llorca, P. Liu, A. Trovarelli, J. A. Rodríguez, S. Colussi and S. D. Senanayake, *ACS Catal.*, 2022, **12**, 12809–12822.

69 L.-P. Merkouri, E. le Sache, L. Pastor-Perez, M. S. Duyar and T. R. Reina, *Fuel*, 2022, **315**, 123097.

70 M. Danielis, S. Colussi, C. de Leitenburg and A. Trovarelli, *Catal. Commun.*, 2020, **135**, 105899.

71 M. Danielis, L. E. Betancourt, I. Orozco, N. J. Divins, J. Llorca, J. A. Rodríguez, S. D. Senanayake, S. Colussi and A. Trovarelli, *Appl. Catal., B*, 2021, **282**, 119567.

72 S. Colussi, A. Gayen, M. F. Camellone, M. Boaro, J. Llorca, S. Fabris and A. Trovarelli, *Angew. Chem., Int. Ed.*, 2009, **48**, 8481–8484.

73 M. Danielis, A. Braga, N. J. Divins, J. Llorca, A. Trovarelli and S. Colussi, *Crystals*, 2023, **13**, 1–16.

74 L.-P. Merkouri, J. L. Martín-Espejo, L. F. Bobadilla, J. A. Odriozola, M. S. Duyar and T. R. Reina, *Nanomaterials*, 2023, **13**, 506.

75 A. Bermejo-López, B. Pereda-Ayo, J. A. Onrubia-Calvo, J. A. González-Marcos and J. R. González-Velasco, *J. CO<sub>2</sub> Util.*, 2022, **58**, 101922.

76 J. Hu, P. Hongmanorom, V. V. Galvita, Z. Li and S. Kawi, *Appl. Catal., B*, 2021, **284**, 119734.

77 A. Bermejo-López, B. Pereda-Ayo, J. A. González-Marcos and J. R. González-Velasco, *J. CO<sub>2</sub> Util.*, 2019, **34**, 576–587.

78 A. Al-Mamoori, A. A. Rownaghi and F. Rezaei, *ACS Sustain. Chem. Eng.*, 2018, **6**, 13551–13561.

79 A. Porta, R. Matarrese, C. G. Visconti, L. Castoldi and L. Lietti, *Ind. Eng. Chem. Res.*, 2021, **60**, 6706–6718.

80 A. S. Al-Fatesh, N. Patel, A. H. Fakieha, M. F. Alotibi, S. B. Alreshaidan and R. Kumar, *Catal. Rev.: Sci. Eng.*, 2023, **66**, 1–99.

81 D. Pakhare and J. Spivey, *Chem. Soc. Rev.*, 2014, **43**, 7813–7837.

82 T. Sasayama, F. Kosaka, Y. Liu, T. Yamaguchi, S. Y. Chen, T. Mochizuki, A. Urakawa and K. Kuramoto, *J. CO<sub>2</sub> Util.*, 2022, **60**, 102049.

83 T. Sasayama, Y. Ono, F. Kosaka, Y. Liu, S. Y. Chen, T. Mochizuki, K. Matsuoka, A. Urakawa and K. Kuramoto, *Sep. Purif. Technol.*, 2025, **354**, 128602.

84 N. D. Charisiou, A. Baklavardis, V. G. Papadakis and M. A. Goula, *Waste Biomass Valorization*, 2016, **7**, 725–736.

85 S. Das, J. Ashok, Z. Bian, N. Dewangan, M. H. Wai, Y. Du, A. Borgna, K. Hidajat and S. Kawi, *Appl. Catal., B*, 2018, **230**, 220–236.

86 T. Stroud, T. J. Smith, E. Le Saché, J. L. Santos, M. A. Centeno, H. Arellano-Garcia, J. A. Odriozola and T. R. Reina, *Appl. Catal., B*, 2018, **224**, 125–135.

87 L.-P. Merkouri, J. L. Martín-Espejo, L. F. Bobadilla, A. Penkova, T. R. Ramirez and J. A. Odriozola, *J. Mater. Chem. A*, 2023, **11**, 13209–13216.

88 L.-P. Merkouri, L. Francisco, J. L. Martín-Espejo, A. Penkova, G. Torres-Sempere, M. Short and M. S. Duyar, *Appl. Catal., B: Environ. Energy*, 2025, **361**, 124610.

89 L. Hu and A. Urakawa, *J. CO<sub>2</sub> Util.*, 2018, **25**, 323–329.

90 M. A. Álvarez, L. F. Bobadilla, V. Garcilaso, M. A. Centeno and J. A. Odriozola, *J. CO<sub>2</sub> Util.*, 2018, **24**, 509–515.

91 L. Proaño, E. Tello, M. A. Arellano-Trevino, S. Wang, R. J. Farrauto and M. Cobo, *Appl. Surf. Sci.*, 2019, **479**, 25–30.

92 L. Proaño, M. A. Arellano-Treviño, R. J. Farrauto, M. Figueiredo, C. Jeong-Potter and M. Cobo, *Appl. Surf. Sci.*, 2020, **533**, 147469.

93 H. Sun, J. Wang, J. Zhao, B. Shen, J. Shi, J. Huang and C. Wu, *Appl. Catal., B*, 2019, **244**, 63–75.

94 S. Sun, S. He and C. Wu, *Chem. Eng. J.*, 2022, **441**, 135752.

95 S. Sun, C. Zhang, S. Guan, S. Xu, P. T. Williams and C. Wu, *Sep. Purif. Technol.*, 2022, **298**, 121604.

96 S. Sun, C. Zhang, S. Chen, X. Zhao, Y. Wang, S. Xu and C. Wu, *R. Soc. Open Sci.*, 2023, **10**, 230067.

97 H. Sun, Y. Zhang, C. Wang, M. A. Isaacs, A. I. Osman, Y. Wang, D. Rooney, Y. Wang, Z. Yan, C. M. A. Parlett, F. Wang and C. Wu, *Chem. Eng. J.*, 2022, **437**, 135394.

98 J. Gandara-Loe, Q. Zhang, J. J. Villora-Picó, A. Sepúlveda-Escribano, L. Pastor-Pérez and T. Ramirez Reina, *Energy Fuels*, 2022, **36**, 6362–6373.

99 Y. Han, M. Tian, C. Wang, Y. Kang, L. Kang, Y. Su, C. Huang, T. Zong, J. Lin, B. Hou, X. Pan and X. Wang, *ACS Sustain. Chem. Eng.*, 2021, **9**, 17276–17288.

100 M. D. Argyle and C. H. Bartholomew, *Catalysts*, 2015, **5**, 145–269.

101 C. H. Bartholomew, in *Catalysis: Volume 10*, Royal Society of Chemistry, 1993, pp. 41–82.

